

## RESEARCH ARTICLE

10.1002/2015JA021877

## Key Points:

- ESF simulations initialized and driven with Jicamarca data
- Simulations able to recover ESF phenomenology
- HF beacons being incorporated to give regional context

## Correspondence to:

D. L. Hysell,  
dlh37@cornell.edu

## Citation:

Hysell, D. L., M. A. Milla, L. Condori, and J. Vierinen (2015), Data-driven numerical simulations of equatorial spread  $F$  in the Peruvian sector 3: Solstice, *J. Geophys. Res. Space Physics*, 120, 10,809–10,822, doi:10.1002/2015JA021877.

Received 3 SEP 2015

Accepted 16 NOV 2015

Accepted article online 19 NOV 2015

Published online 15 DEC 2015

Data-driven numerical simulations of equatorial spread  $F$  in the Peruvian sector 3: SolsticeD. L. Hysell<sup>1</sup>, M. A. Milla<sup>2</sup>, L. Condori<sup>2</sup>, and J. Vierinen<sup>3</sup>

<sup>1</sup>Earth and Atmospheric Sciences, Cornell University, Ithaca, New York, USA, <sup>2</sup>Jicamarca Radio Observatory, Lima, Peru, <sup>3</sup>MIT Haystack Observatory, Westford, Massachusetts, USA

**Abstract** We present results from a continuing effort to simulate equatorial spread  $F$  (ESF) using observations from the Jicamarca Radio Observatory near Lima, Peru. Jicamarca measures vertical and zonal plasma drifts along with plasma number density profiles overhead. The number density profiles are used to initialize a three-dimensional regional model of the ionosphere capable of simulating plasma density irregularities produced during ESF conditions. The vertical drifts measurements are used to drive the numerical simulation continuously. Neutral winds are derived from the new Horizontal Wind Model '14 (HWM-14) model, and the zonal winds are scaled so as to make the zonal plasma flows at the start of the simulation agree with the ISR profile measurements. Coherent scatter radar imagery from Jicamarca is used to validate the simulation results. Campaign data were collected in April and December 2014, and a few events representative of low and high ESF activity were selected for analysis. The numerical simulations are able to reproduce the level of activity observed along with the gross features of the ESF irregularities and radar plumes. Data from a network of HF beacons are being incorporated into the forecast analysis in order to elucidate radar plumes which sometimes appear even when the simulation fails to predict them.

## 1. Introduction

Equatorial spread  $F$  (ESF) is a common, spectacular, and disruptive space weather phenomenon that occurs in the nighttime equatorial  $F$  region ionosphere during both geomagnetically quiet and disturbed times. ESF is caused by low-frequency plasma instabilities driven by the free energy in the postsunset configuration of the ionosphere. It is characterized by broadband plasma density irregularities spanning scale sizes from tens of centimeters to hundreds of kilometers or more. In latitude, the irregularities can extend all the way to the midlatitude ionization anomalies and perhaps beyond. The irregularities interfere with transionospheric radio signals and pose a hazard to communication, navigation, and imaging systems. ESF is visible to a number of different ground-based instruments which can be used to monitor irregularity occurrence and associated plasma flows (see recent review by Kelley *et al.* [2011]).

The state of ESF research was summarized by Woodman [2009] who proposed that the main physical mechanisms at work in ESF are now well understood. This is the third in a series of papers intended to test Woodman's proposition by combining observations with numerical simulations in the Peruvian sector [see also Hysell *et al.*, 2014a, 2014b]. The tests have been conducted in the following way. First, the most important ionospheric state parameters, plasma number density profiles, vector electric field profiles, and zonal thermospheric winds, are measured at the Jicamarca Radio Observatory near Lima, Peru, operating in campaign mode. Representative events from each campaign when ESF did or did not occur are chosen for further analysis, mainly on the basis of data quality. The measurements are then used to initialize and drive regional, three-dimensional numerical simulations of ESF. The simulations account for the essential features of instability in the collisional regime including the destabilizing effects of vertical currents associated with differential zonal plasma and neutral flows [Hysell and Kudeki, 2004; Kudeki *et al.*, 2007]. Finally, the simulation results are compared with radar imagery of ESF irregularities and plumes observed with coherent scatter. Woodman's proposition is supported to the extent that the numerical simulations can reproduce the occurrence (or nonoccurrence) of ESF plumes, the times they appear, their rates of development, and their altitudes and morphologies.

Experimental campaigns were conducted at Jicamarca in December 2012; April and September 2013; April, November, and December 2014; and in February 2015. Hysell *et al.* [2014a, 2014b] considered observations

from April and September 2013, respectively, i.e., equinox conditions. They demonstrated that it is possible to reproduce the ESF plumes that appear in nature through numerical simulations initialized and driven by ionospheric observations at a single site. Crucially, the simulations produced no “false alarms” or predictions of plumes that did not actually occur. This indicates that no key ingredient or necessary condition for ESF is being neglected in the numerical model. Occasionally, plumes were observed in nature that were not predicted by the numerical simulation on days when the conditions seemed inauspicious for ESF. These “rogue plumes” may simply have been transported into the Peruvian sector from longitude or time sectors where conditions were more favorable. They may also have been produced by mechanisms not accounted for in the numerical model, by “sufficient conditions” outside of the scope of the model.

This paper continues the investigation by considering data from solstice periods. The June solstice period is especially interesting in the Peruvian sector since ESF occurs only rarely then. The ability of a numerical simulation to predict the absence of irregularities is crucial for testing our understanding of the phenomenon but is a capability that often goes unreported in the literature. Below, we report on campaign data representing solstice conditions in 2014 at Jicamarca, on attempts to reproduce them in simulation and on the implications for Woodman’s proposition.

## 2. Campaign Data

Ionospheric observations were made at the Jicamarca Radio Observatory in late April and December 2014 under geomagnetically quiet conditions when the  $F_{10.7}$  solar flux index was about 130 and 200, respectively. A new mode was in use at Jicamarca which measures plasma number density and vector drift profiles simultaneously. Radar images of ionospheric irregularities can also be constructed from spaced-receiver coherent scatter data collected at the same time as the incoherent scatter data [Hysell and Chau, 2006]. The combined mode utilizes 4 different transmitters along with 16 distinct receivers. For a more detailed description of the experimental modes in use in these campaigns, see Hysell *et al.* [2014a, 2014b].

In our previous studies, thermospheric wind estimates from red line Fabry Perot interferometers at Jicamarca and/or Arequipa, Peru, were available for analysis. That is not the case for the solstice experiments considered. Observing conditions are generally poor in December solstice, during local summer, and deprive us of usable wind estimates in December as a rule. While observing conditions are generally good during June solstice, the ionosphere was too high in the postsunset sector throughout our April campaigns to yield usable Fabry Perot measurements. We consequently turn to other experimental means based entirely on radar observations for estimating the thermospheric winds in the simulation studies (see below).

Measurements were made between 22 and 25 April 2014, when ESF irregularities occur rarely [e.g., Aveiro and Hysell, 2010]. Figure 1 shows Jicamarca data which are representative of the April campaign and of June solstice conditions generally. In fact, no  $F$  region ionospheric irregularities were detected on 24/25 April. Even the so-called “bottom-type” layers, which are nearly ubiquitous in the postsunset  $F$  region, were absent [see Woodman and La Hoz, 1976]. Consequently, the incoherent scatter plasma density and drifts measurements were completely uncontaminated by coherent scatter radar clutter.

Figure 1 (top, first panel) shows the plasma number density in the postsunset period. The postsunset rise and subsequent fall of the ionosphere is obvious. To the right is another panel showing an electron density profile at 2330 UT (1830 LT). This will be the start time for the numerical simulations described later in the manuscript. A dashed line in the same panel shows the density profile predicted by the Parametrized Ionospheric Model (PIM) at Jicamarca’s longitude at 2330 UT assuming an  $F_{10.7}$  solar flux index of 250 (see Daniell *et al.* [1995] for a description of the PIM empirical model). As is the case here, we find that PIM can usually be made to reproduce actual ionospheric conditions over Jicamarca at sunset given a suitably chosen (if possibly inaccurate) setting for  $F_{10.7}$ .

Figure 1 (top, second panel) shows the zonal plasma drifts measured over Jicamarca. As is generally the case in the evening, the flow is eastward except in the bottomside where slow westward flows are visible [see, e.g., Kudeki *et al.*, 1981; Tsunoda *et al.*, 1981; Haerendel *et al.*, 1992]. The zonal flow speed increases with time. While shear is often assumed to stabilize the bottomside ionosphere [e.g., Guzdar *et al.*, 1983; Satyanarayana *et al.*, 1984; Hassam, 1992], the picture is actually more complicated than first thought [Fu *et al.*, 1986; Flaherty *et al.*, 1999; Hysell and Kudeki, 2004]. As mentioned above, analyses and simulations carried out to date indicate

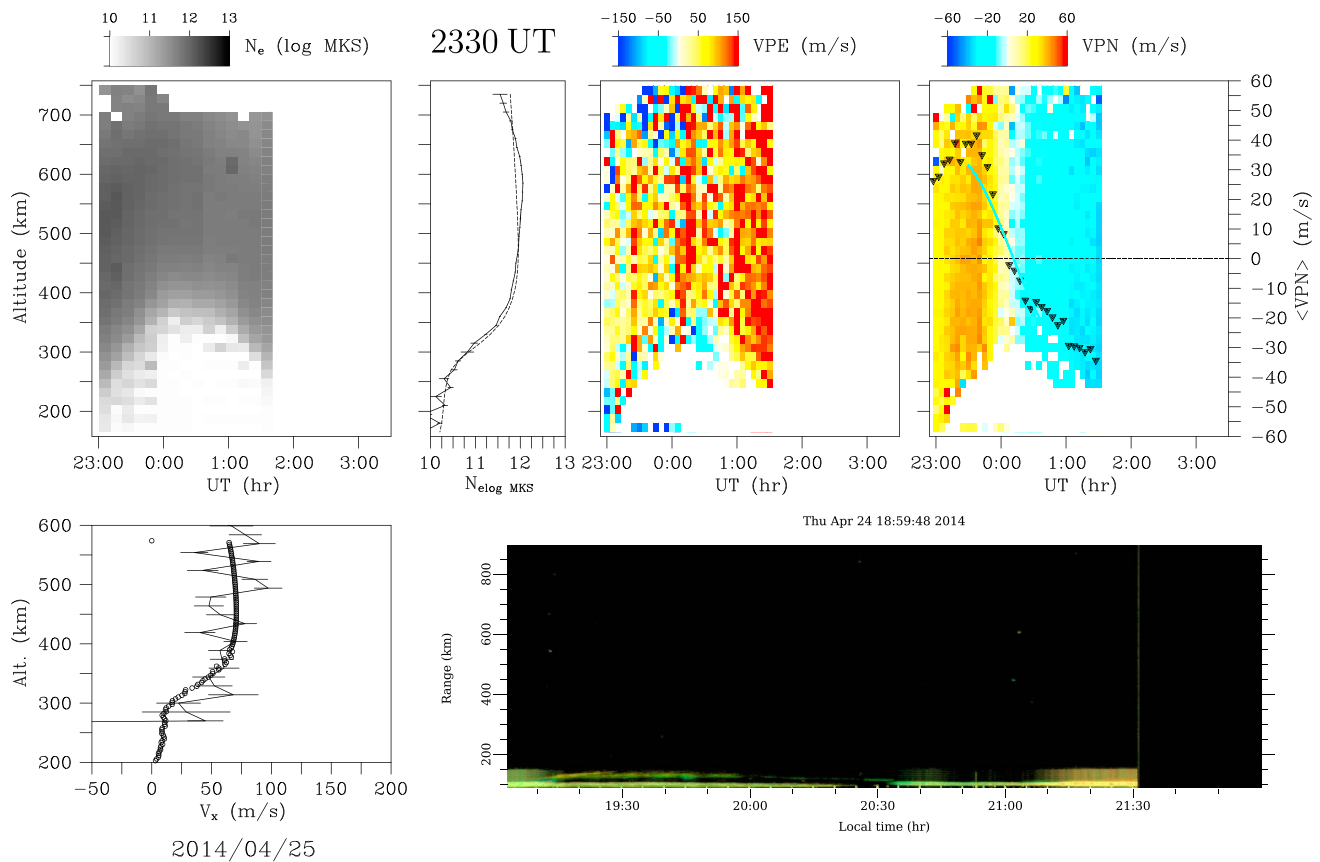


**Figure 1.** Jicamarca observations of ESF 24/25 April 2014. (top): (first panel) electron density, (second panel) electron density profiles at 2330 UT, (third panel) zonal plasma drifts, and (fourth panel) vertical plasma drifts. (bottom left) Measured zonal plasma drift profiles at 2330 UT (solid line with error bars) together with the computed drift profile (plotted points) at the start of the numerical simulation. (bottom right) Coherent backscatter. Note that UT = LT + 5 h.

that the vertical currents associated with differential plasma and neutral zonal flows are highly destabilizing around twilight and can be essential for producing large-amplitude irregularities within an hour of sunset.

Figure 1 (top, fourth panel) shows the vertical plasma drift profiles along with the height-averaged drift, indicated by marker symbols. The prereversal enhancement of the drifts is clearly evident. The time of reversal (from ascent to descent) was approximately 0 UT (1900 LT). Plasma ascent was unseasonably rapid after sunset, which is why such an anomalously large value for the  $F_{10.7}$  parameter was required for PIM to reproduce the density profile measured at 2330 UT.

Figure 1 (bottom left) shows the zonal plasma drift profile from radar measurements averaged over an interval centered on 2330 UT (1830 LT). Also shown is the zonal plasma drift profile computed during the initial time step of the numerical simulation of this event. As will be described later, the neutral winds used in the simulation are based on an empirical model and, in the case of the zonal winds, scaled to achieve congruity between the measured and simulated zonal plasma drifts at the start of the simulation. This procedure is used in lieu of actual thermospheric wind measurements.

Figure 1 (bottom right) shows coherent scatter intensity in range-time-intensity format. No F region coherent scatter was observed on 24/25 April, marking the event as an extremely inactive one.

Figure 2 shows observations like those in Figure 1 except for the previous day. We were fortunate to have captured even one active ESF event in late April. This time, a bottom-type scattering layer appeared at 0010 UT (1910 LT) followed by the passages of a high-altitude radar plume beginning at about 0045 UT (1945 LT). The plasma irregularities produce radar clutter and contaminate the incoherent scatter data, causing gaps in the record at certain altitudes and times. It was, nonetheless, possible to measure an uncontaminated electron density profile at 2330 UT as well as the time history of the average vertical plasma drifts. The vertical drifts were very large on this night, reaching almost 50 m/s at 2330 UT, and remained upward through about

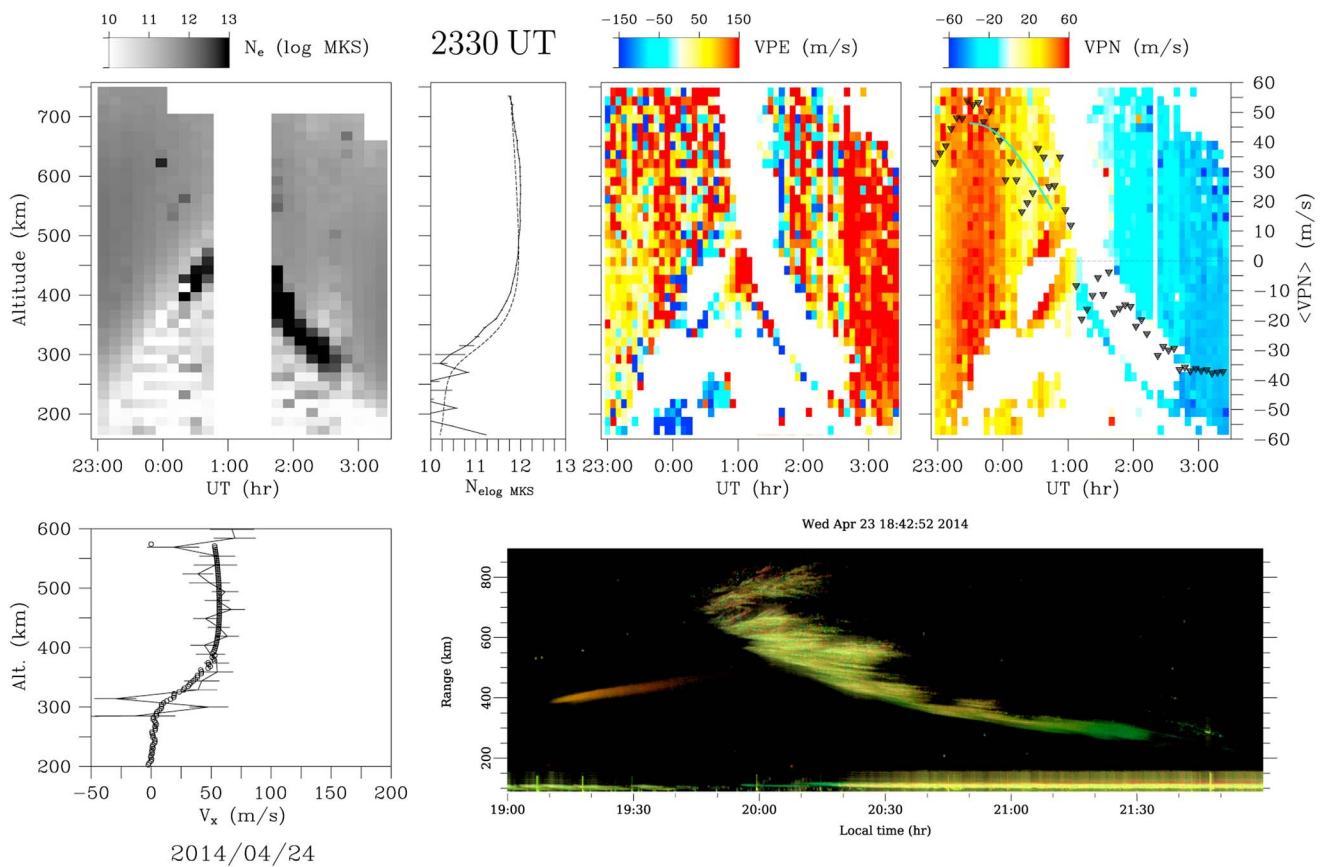


Figure 2. Same as Figure 1 except for 23/24 April 2014.

0100 UT (2000 LT) or about an hour longer than on 24 April. The unseasonably strong and sustained upward drifts were undoubtedly responsible for the high level of ESF activity. The large postsunset drifts elevated the *F* region so much that by 2330 UT, the profile became impossible to reproduce completely accurately using PIM for any choice of the  $F_{10.7}$  model parameter. The PIM profile shown here was calculated using and  $F_{10.7}$  parameter of 250.

Another campaign was conducted at Jicamarca between 15 and 21 December 2014. Note that sunset occurs one half hour later in December than in April, a fact which is considered in the numerical simulations. As pointed out above, the solar flux was much higher in December than in April, and the shapes of the plasma density profiles were consequently different; the postsunset valley region exhibiting much larger plasma density in December than in April. In accordance with the climatology for the sector established by *Scherliess and Fejer [1999]*, the vertical plasma drifts were also more robust in December than in April on average, with the reversal time occurring much later in December. Irregularities were observed on each night of the December campaign, taking the form either of large radar plumes or a mixture of bottom-type and bottomside layers. Below, we consider one example of each of the two possible outcomes.

Figure 3 shows observations for 17/18 December 2014. This event features a bottom-type scattering layer between 0050 and 0120 UT (1950 and 2020 LT). This was replaced by a bottomside layer between 0120 and 0215 UT (2020 and 2115 LT) which was followed immediately by a radar plume, which appeared late. (A bottomside layer is distinguished from a bottom-type layer by its greater degree of vertical development.) A very small radar plume seems to have passed over the observatory at 0120 UT (2020 LT).

The ionosphere ascended vigorously until about 0130 UT (2030 LT). By 2400 UT, the ionospheric density profile was exhibiting a secondary peak above 500 km altitude. This peak, reminiscent of the so-called F3 layer described by *Balan et al. [1997, 1998]*, cannot be reproduced by the PIM model and reflected in our simulation study. We do not believe it to be a critical feature for the development of ESF, however, which emerges from the bottomside. The bottomside profile in this case is well reproduced by PIM using an  $F_{10.7}$  parameter of 180.

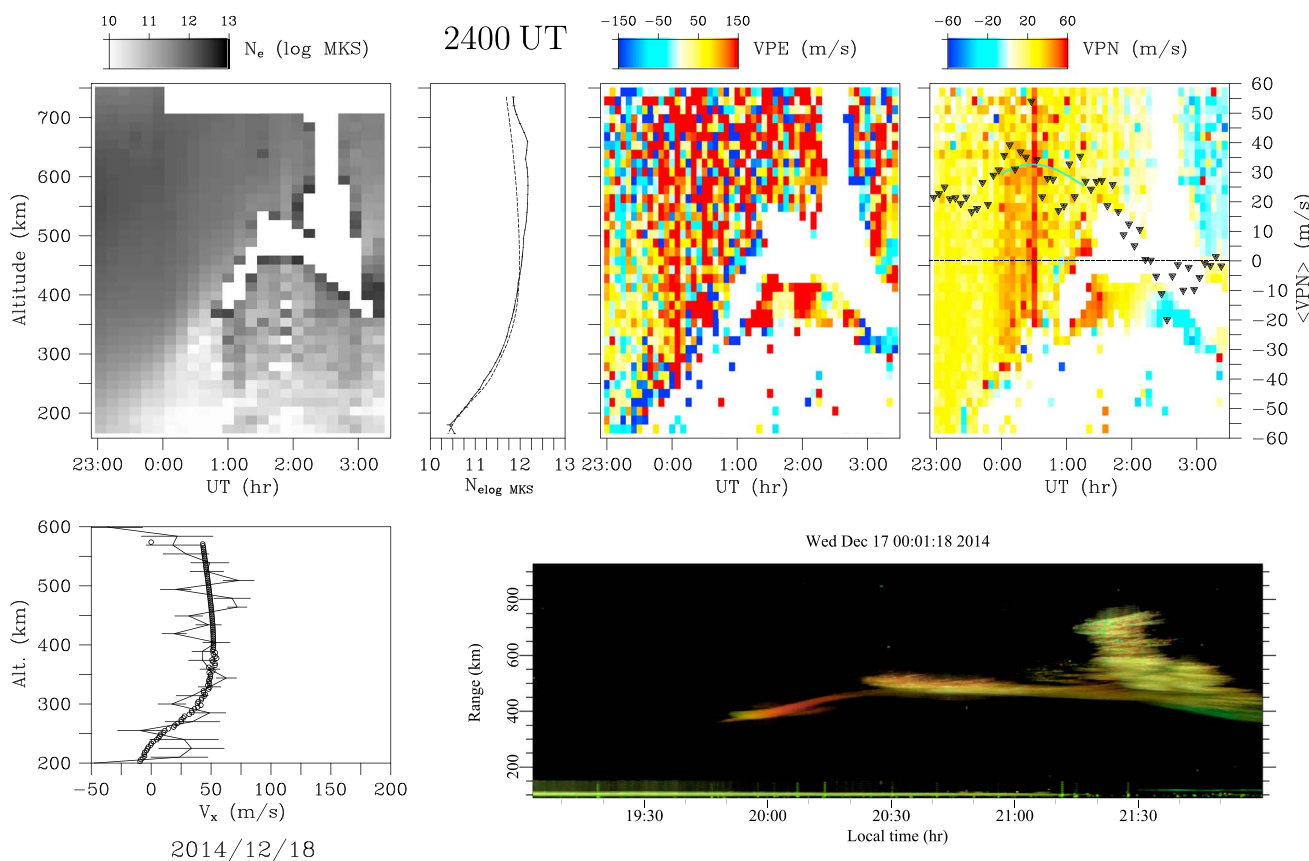


**Figure 3.** Same as Figure 1 except for 17/18 December 2014. Note that the start time for the December simulations is 2400 UT (1900 LT).

Lastly, Figure 4 shows campaign data for 19 December 2014, an event featuring a series of spectacular ESF radar plumes. This event is characterized by exceptionally large and persistent upward plasma drifts which exceeded 50 m/s at about 0030 UT (1930 LT), about the time of the first appearance of a bottom-type scattering layer. Radar plumes appeared subsequently shortly after 0100 UT (2000 LT), persisting for about two hours. As in the previous example, the density profile measured at 2400 UT exhibited a secondary or “F3” layer, only the layer is even more pronounced this time. The bottomside density profile at this time could be reproduced by PIM with the choice of 200 for the  $F_{10.7}$  parameter.

### 3. Numerical Simulation

We turn here to numerical simulations of the Jicamarca campaign data. The numerical model and algorithms used for the simulation have been described in detail in *Hysell et al.* [2014a, 2014b]. The simulation considers the spatiotemporal evolution of four ion species— $O_2^+$ ,  $NO^+$ ,  $O^+$ , and  $H^+$ —in three dimensions in a tilted magnetic dipole coordinate system. The electrostatic potential is found by solving the quasi-neutrality condition ( $\nabla \cdot \mathbf{J} = 0$ ) which considers Pedersen, Hall, and direct conductivities as well as currents driven by winds, pressure, and gravity. The equipotential magnetic field line approximation is not made. The quasi-neutrality condition is solved using a preconditioned biconjugate gradient method. Explicit expressions for the drifts of the ion species in the collisional regime are then used to update the ion number densities via second-order monotone upwind schemes for conservative laws [see *Trac and Pen*, 2003, for review]. Charge exchange and dissociative recombination chemistry is accounted for.

The simulation draws initial and background parameters from a combination of empirical models tuned to reflect day-to-day variability in the campaign data. As alluded to earlier, we use the PIM model to initialize the electron number density throughout the simulation space. A model is necessary here because our simulation requires initialization over a broad span of locations and local times and not just the places and local times when measurements are available. We feed PIM a proxy value of the F10.7 solar flux index so that it predicts

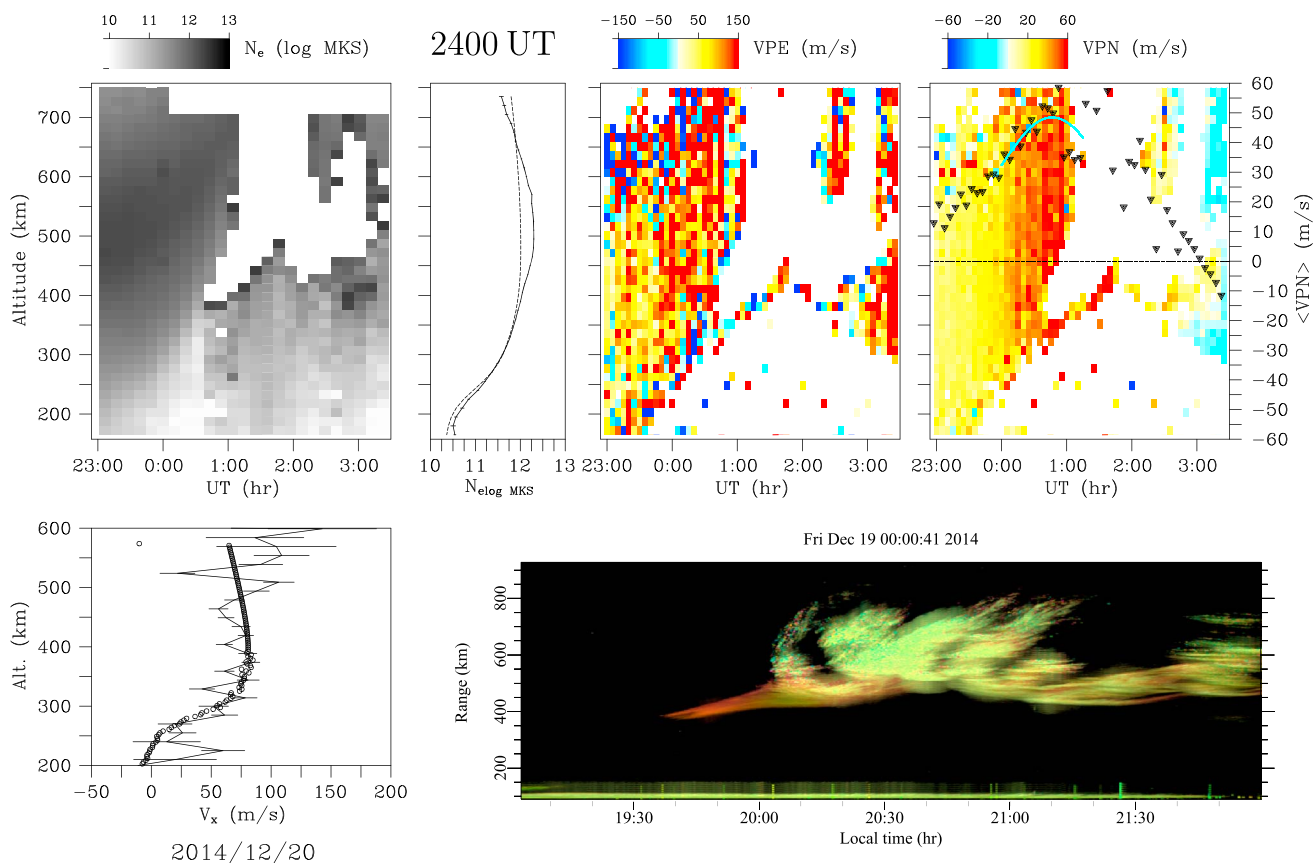


**Figure 4.** Same as Figure 1 except for 19/20 December 2014. Note that the start time for the December simulations is 2400 UT (1900 LT).

a number density profile which is congruent with the radar data at the start of the simulation. The initial ion composition is taken from the IRI-2007 model [Bilitza and Reinisch, 2008]. Neutral parameters necessary for calculating ion- and electron-neutral collision frequencies are taken from the NRLMSISE-00 model [Picone et al., 2002]. The neutral parameters from NRLMSISE-00 are updated dynamically throughout the simulation. The background zonal electric field used in the simulation is specified according to the ISR vertical drifts measurements. We fit the height-averaged vertical drifts from 2300–0200 UT (1800–2100 LT) to the formula

$$v_d(t) = v_o + v_1 \sin \left( 2\pi \frac{t - t_o}{\tau} \right)$$

where  $t$  is universal time in hours,  $v_o$  is a baseline,  $v_1$  is a perturbation amplitude,  $\tau$  is a period, and  $t_o/\tau$  sets the phase. We then set the background zonal electric field in the simulation according to  $v_d$ . This simple model generally captures the vertical drifts in the interval surrounding the prereversal enhancement well without admitting observation noise into the simulation. See the cyan curves in Figures 1–4 for the curve fits for the simulation times in question.

Finally, the neutral winds in the simulation are provided by the new Horizontal Wind Model '14 (HWM14) model [Drob et al., 2015]. The new version of the HWM model has been shown to reproduce ground-based Fabry Perot interferometer data from the American sector much more accurately than older versions of the model. The model winds are rescaled in our simulations in order to account for day-to-day variability. Specifically, the zonal neutral winds are scaled by a single, constant factor meant to optimize congruity between the predicted and measured zonal plasma drift profiles at the initial time of simulations. (The meridional winds are imported but not scaled.) We refer to the multiplicative scaling constant below as  $s$ .

Table 1 gives the parametrizations used for the simulation runs. Note, finally, that longitude variations in all of the aforementioned parameters, the background neutral winds and zonal electric fields notably, are set to match their local time variations when no other basis for specification exists.

**Table 1.** Parameters Used to Initialize and Force ESF Simulations Corresponding to Data From the Jicamarca Solstice Campaigns

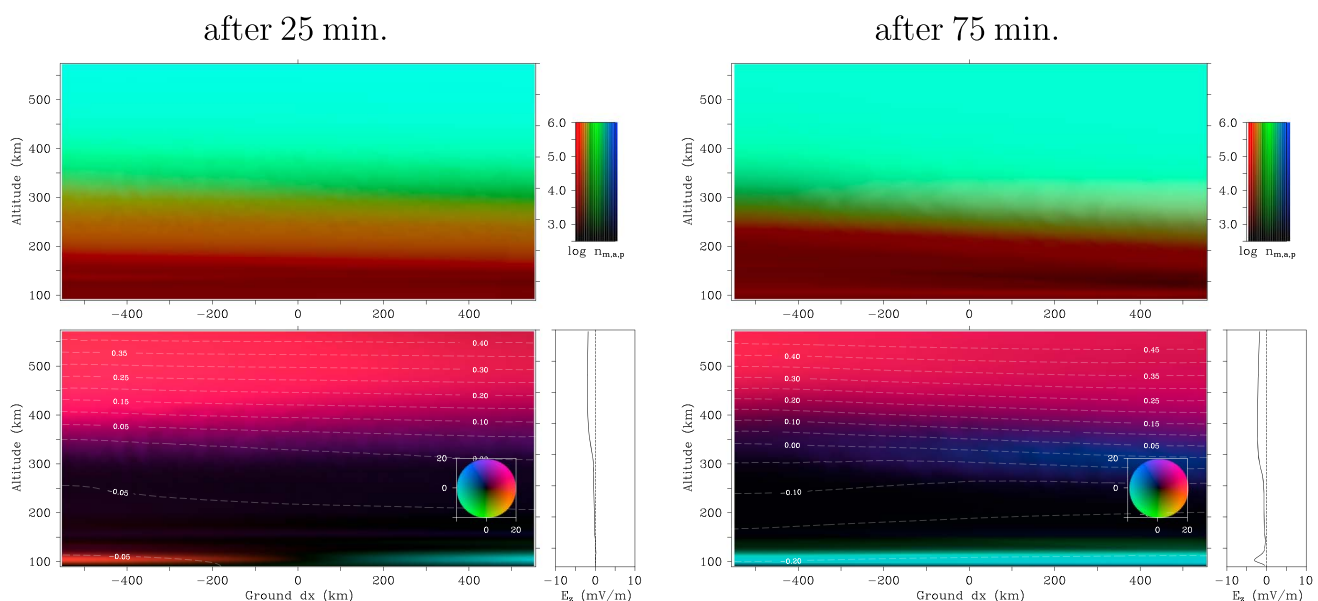
Event	PIM $F_{10.7}$	$s$	$v_o$	$v_1$	$t_o$	$\tau$
Apr 24	250	1.0	2.3	32.7	22.3	3.7
Apr 23	250	0.9	13.7	32.5	22.2	5.3
Dec 17	180	0.8	25.2	7.1	23.7	3.1
Dec 19	200	1.0	32.4	16.1	24.0	3.1

Figure 5 shows simulation results for 24 April, the very low activity event typical of June solstice in the Peruvian sector. The panels on the left and right sides of the figure depict simulation times 25 and 75 min into the run, respectively, which began at 2330 UT (1830 LT). The top panel in each case shows plasma number density and composition in the equatorial plane, and the bottom panel shows current density and electrostatic potential, also in the equatorial plane.

The simulation of the low-activity event produced essentially no ionospheric irregularities. The zonal electric field was eastward but modest at the start of the simulation and reversed direction within the first 15 min of the run. Thereafter, the field and associated Pedersen currents were westward. This configuration is highly stable in the bottomside  $F$  region. Only at higher altitudes, near and above the  $F$  peak, did eastward currents driven by gravity overcome the westward Pedersen currents. This is too high to be relevant for irregularity production, however.

In contrast, Figure 6 shows simulation results for the high-activity event of the April 2014 campaign. After 25 min, the  $F$  layer in the 23/24 April simulation ascended noticeably farther than it had in the 24/25 April simulation. The upward tilt in the layer from west to east, from earlier to later local times, is an indicator of continuing, rapid ascent. After just 25 min, distinct plasma density irregularities formed in the strata between about 350–400 km altitude. This matches the height range where bottom-type layers emerged initially in the campaign data. This altitude range is also coincident with the region of vertical current which is signified by violet hues in the transverse current density panel.

By the 75 min time step (0045 UT, 1945 LT), the  $F$  layer ascended further, and irregularities grew, developed, and ascended to altitude strata where the current was mainly eastward and strong. The irregularities



**Figure 5.** Numerical simulation of events on 24/25 April 2014 (low activity) initialized at 2330 UT. (left and right) Simulated results after 25 and 75 min, respectively. (top row) Plasma number density, with red, green, and blue tones representing molecular, atomic, and protonic ion abundances, respectively. (bottom row) Vector current density in the equatorial plane in  $\text{nA}/\text{m}^2$  according to the circular legend shown. White lines are equipotentials, approximate streamlines of the flow. The vertical electric field through the midpoint of the simulation is plotted in profiles to the right of the current density plots. Note that diamagnetic currents have no effect on dynamics and are not included in the current densities shown.

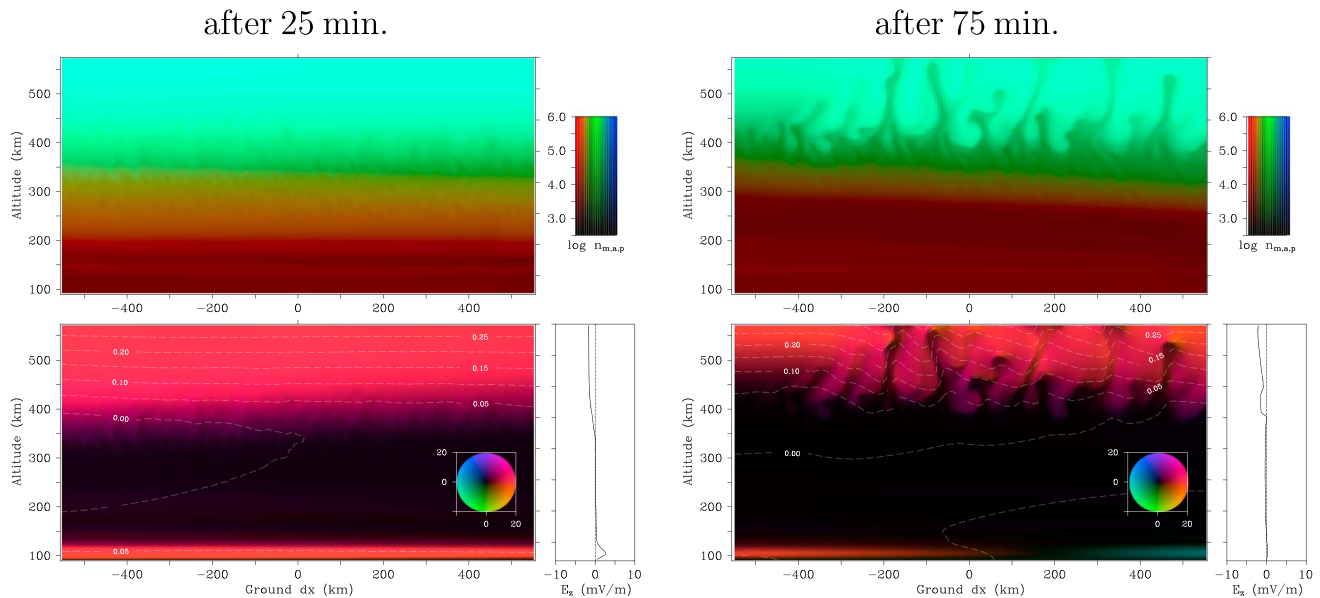


**Figure 6.** Same as Figure 5 except for 23/24 April 2014 (high activity).

penetrated into the topside and through the upper boundary of the simulation space in some cases. The simulation reproduced the topside plumes clearly evident in the campaign data which ascended to 700 km by 0045 UT (1945 LT) when they first drifted over the radar.

Turning to December solstice, Figure 7 shows simulation results for the relatively low-activity event. The panels on the left and right sides of the figure depict simulations times 25 and 75 min into the run, respectively, which began at 2400 UT (1900 LT). The December solstice campaign data were characterized by electron density profiles which were less rarefied in the valley region than in April and by larger and longer-lived postsunset vertical drifts. Both of these features are evident in Figure 7 which shows a fairly dramatic upward tilt from west to east, from early to late local times. Bottomside recombination also causes the  $F$  region on the eastern side of the simulation space to be much steeper than on the western side. Plasma shear flow in the bottomside is much stronger in the December simulations than in the April simulations.

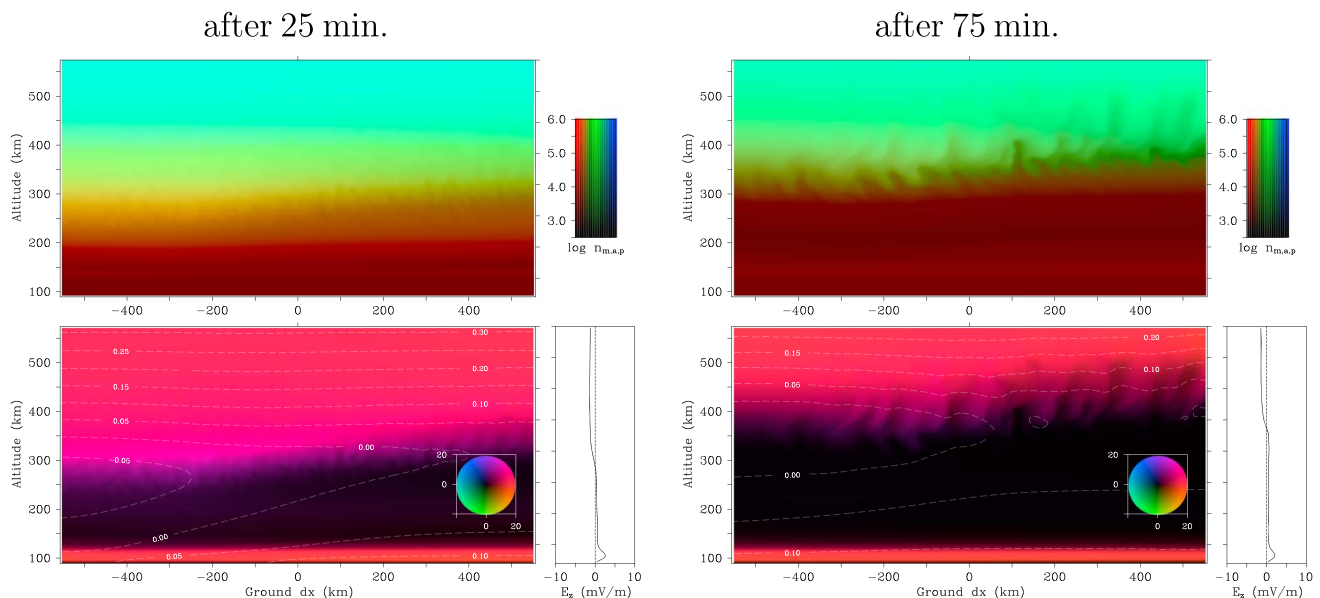


**Figure 7.** Same as Figure 5 except for 17/18 December 2014 (low activity). Note that the simulation is initialized at 2400 UT.



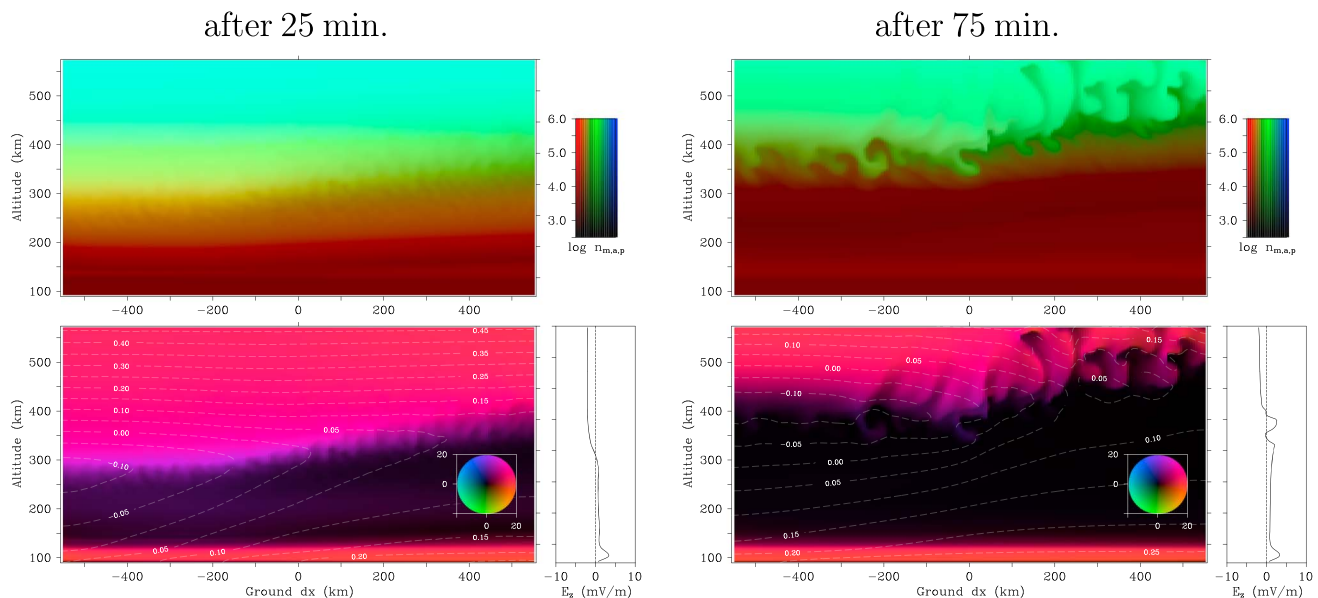


**Figure 8.** Same as Figure 5 except for 19/20 December 2014 (high activity).

By the 75 min time step (0115 UT, 2015 LT), distinct irregularities are evident in the center of the simulation in the bottomside, concentrated mainly between 300 and 400 km altitude. This corresponds roughly to the time when a bottom-type layer was observed over Jicamarca in the same altitude range. In subsequent simulation times, the irregularities continue to ascend and to develop slowly. In nature, the irregularities ascended and developed vertically until the vertical drifts reversed sign around 0200 UT (2100 LT). The radar plume that passed over Jicamarca starting at 2130 LT was presumably produced originally far to the west of the facility at an earlier time. The simulations for this event are consistent with plume production given enough time for irregularity development.

Finally, Figure 8 shows simulation results for the high-activity December solstice event. The conditions for this simulation were not very different from the low-activity December event except mainly for the fact that the background vertical drifts increased steadily over time, reaching approximately 50 m/s by the end of the simulation run. Figure 8 (left column) are nearly indistinguishable from those on the left side of Figure 7. In nature, the two events unfolded along similar lines initially.

However, by the 75 min mark (0115 UT, 2015 LT), the simulation was predicting fast-rising depletions that were already penetrating into the topside and through the upper simulation boundary in the eastern side of the simulation space. The depletions in the central portion of the space encountered the upper boundary at about 70 min., preventing them from ascending further. The simulation therefore anticipated the radar plumes in Figure 4 which drifted over the simulation first at about 0110 UT (2010 LT).

#### 4. Radar Imagery

In tandem with the incoherent scatter radar observations, coherent scatter experiments are performed at Jicamarca that utilize one small antenna module for transmission and eight identical modules for reception. The half-power full beam width of each module is approximately  $6^\circ$ . Information in the range-time-intensity (RTI) panels in Figures 1–4 above are derived from the coherent scatter radar mode using conventional analysis wherein the power from the eight antenna modules is simply added. The rather broad beam width of the antennas involved causes the RTI plots to suffer from rather severe beam broadening effects. By applying aperture synthesis methods to the full data covariance matrix, however, true images of the backscatter (backscatter power versus range, bearing, Doppler frequency, and time) can be formed [see, e.g., *Hysell and Chau, 2006*]. The angular resolution of the imagery is governed by the Shannon-Hartley theorem and can be much finer in practice than the beam width of Jicamarca's main array [*Kosarev, 1990*]. Radar imaging mitigates spatiotemporal ambiguity in coherent scatter data analysis and facilitates an unbiased appraisal of irregularity morphology.

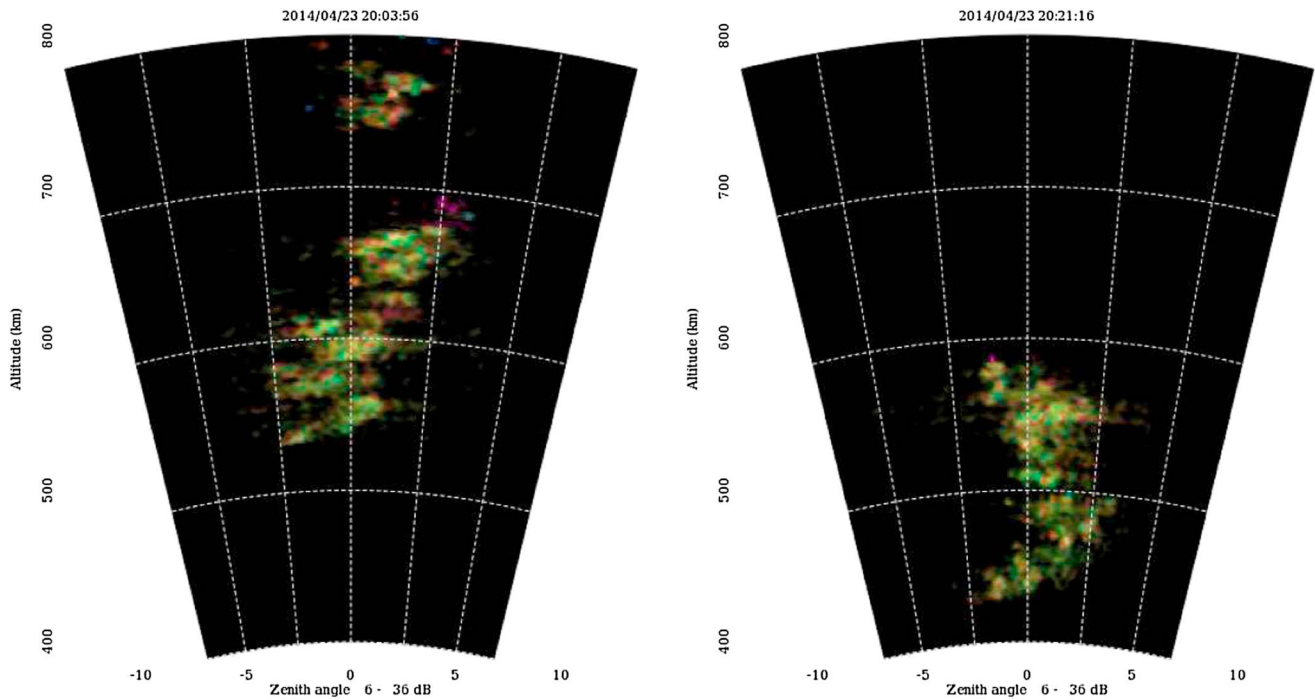


**Figure 9.** Aperture synthesis radar imagery for 23 April 2014 (high-activity case).

Radar images for two distinct radar plumes observed on 23 April 2014 are shown in Figure 9, while three of the several plumes observed in 19 December 2013 are shown in Figure 10. The images depict signal-to-noise ratio versus range and azimuth in the equatorial plane given an incoherent integration period of about 10 s. The signal-to-noise ratio is represented by the brightness of the pixels in the image in dB in the range indicated. The hue and saturation of the pixels reflect Doppler spectral information, but we make no attempt to interpret that information in this instance since most of the echoes are strongly frequency aliased. The resolution of the pixels is finer than 1 km × 1 km. Animated sequences of images (not shown) reveal that the irregularities in question are undergoing creation and destruction while moving in an inhomogeneous flow field, i.e., not simply frozen into a uniform background flow.

In previous experiments, we have found that backscatter at this spatial scale arrives from the most deeply depleted regions and channels within the irregularities and so delineate the gross irregularity structure [Hysell *et al.*, 2009]. There is therefore some basis for comparison between these images and the numerical simula-

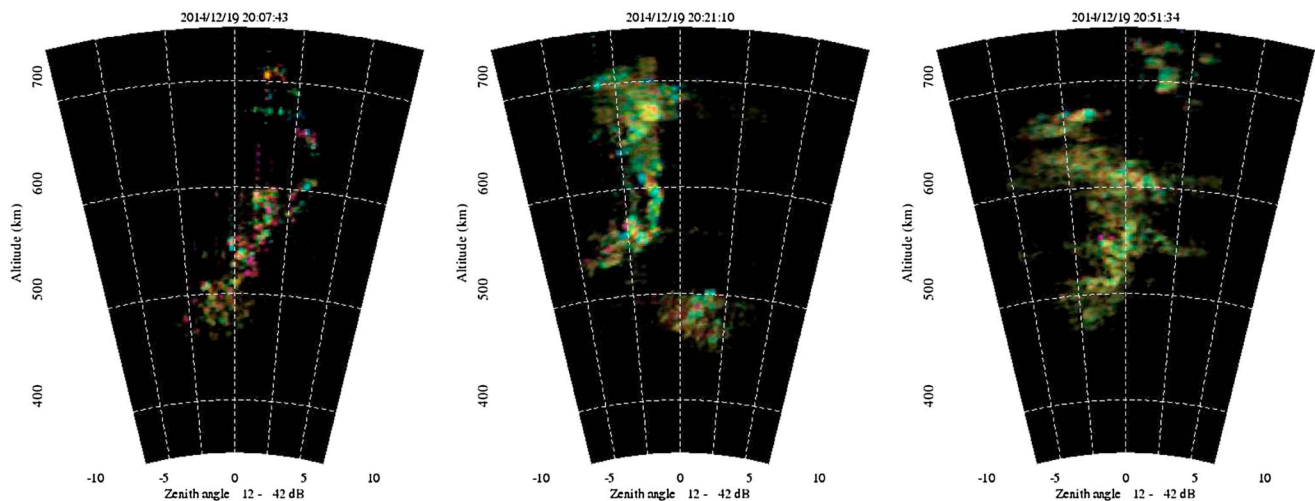


**Figure 10.** Aperture synthesis radar imagery for 19 December 2014 (high-activity case).

tions. However, coherent scatter signifies the presence of plasma density irregularities at the Bragg scale only and so the correspondence is imperfect at best.

The radar plumes in Figures 9 and 10 are typical of ESF, manifesting backward "C" shapes, narrow vertical channels, and a high degree of structuring indicating secondary interchange instability driven mainly by zonal winds. The plumes exhibit modest tilts from the vertical and occasionally bifurcate. The width of the imaged region is approximately 100 km at 600 km altitude which is sufficient to contain one or sometimes two different plumes. Comparison with Figures 6 and 8 reveals these characteristics to be shared by the radar plumes that develop in simulation.

## 5. HF Beacons

In a number of campaigns spanning different seasons and solar activity levels, numerical simulations have been shown to be able to anticipate the occurrence of ESF plumes on the basis of electron density profiles and vector plasma drifts measured overhead at Jicamarca. Occasionally, plumes have been observed when the conditions were not conducive to plume formation according to the simulations. In order to investigate the proposition that these plumes were generated far outside the region being simulated, a network of HF beacons is being installed in the Peruvian sector. HF radio propagation will be used to monitor the advection of ionospheric irregularities across the region outside the volume probed by the Jicamarca ISR.

The beacon network presently consists of a transmitter at Ancon (11°46'37"S, 77°09'1"W, 51 meters above sea level (masl)) and receivers at Jicamarca (11°57'5.8"S, 76°52'27"W, 510 masl) and Huancayo (12°02'30"S, 75°19'15"W, 3315 masl), Peru. Two frequencies are being used: 2.72 and 3.64 MHz. The transmitter emits CW signals with pseudo-random binary phase codes with 10  $\mu$ s baud lengths and a long repetition time (100 ms). Upon decoding, the group delays of the signals can thus be determined. Doppler information indicative of the time rate of change of the phase delays of the signals is also available from the analysis. Finally, reception is performed using a pair of spaced receivers. Information about the arrival bearing of the signals is therefore available through the use of interferometry. Satisfactory single-hop (and sometimes double-hop) signals can be retrieved using low-power levels of the order of 1 W, while multiple hops are visible using higher-power levels.

Example HF data corresponding to the April 2014 campaign discussed above are shown in Figure 11. The O and X mode traces mainly overlap in the data although they are sometimes slightly separated. Backscatter from equatorial electrojet irregularities dominates during the day when the *E* or *Es* layer is blanketing and/or absorption causes *F* layer reflections to be attenuated. The *F* layer traces become visible at about 1500 LT each day and remain so until about 0900 LT the following day.

The virtual heights of the traces ascend rapidly starting at about 1830 LT when the bottomside layer undergoes rapid recombination. On 24 April, the low-activity event, the virtual height began decreasing at about 1900 LT, the time when the vertical drifts measured by the ISR reversed. On 23 April, the high-activity event, the virtual height was still increasing at 1910 LT when range spreading first appeared. This is the time when the bottom-type scattering layer appeared in the Jicamarca observations. Range spreading accompanied by large Doppler shifts became more aggravated after 1945 LT when a radar plumes began passing over Jicamarca.

Although there is some fine structure in the single-hop traces in both events just prior to sunset, there are no obvious precursors to ESF in the 23 April traces that are absent in the traces from 24 April. Similar remarks hold for the HF data from the December campaign. However, the accumulating beacon data set does show examples of waves and solitary perturbations in the traces recorded around twilight. Analysis of the expanding data set might help to eliminate what discrepancies remain between ESF simulations and observations.

A numerical code has been developed to estimate the state of the ionosphere by applying statistical inverse methods to the beacon data. The ionosphere is modeled in the vertical by a Chapman function specified by three parameters. These parameters are specified horizontally using bicubic B spline interpolation on a large grid. Through the model ionosphere, rays are traced in the paradigm of geometric optics using an updated version of the methodology of *Jones and Stephenson* [1975]. The ray connecting the transmitter and receiver is determined iteratively for the given model ionosphere using a shooting method. Finally, the model ionosphere is updated iteratively using a Levenberg Marquardt algorithm that minimizes the discrepancy between the observed and predicted group delays while also minimizing the global horizontal curvature of the model. Incorporating Doppler shift and interferometry information is straightforward since those characteristics are

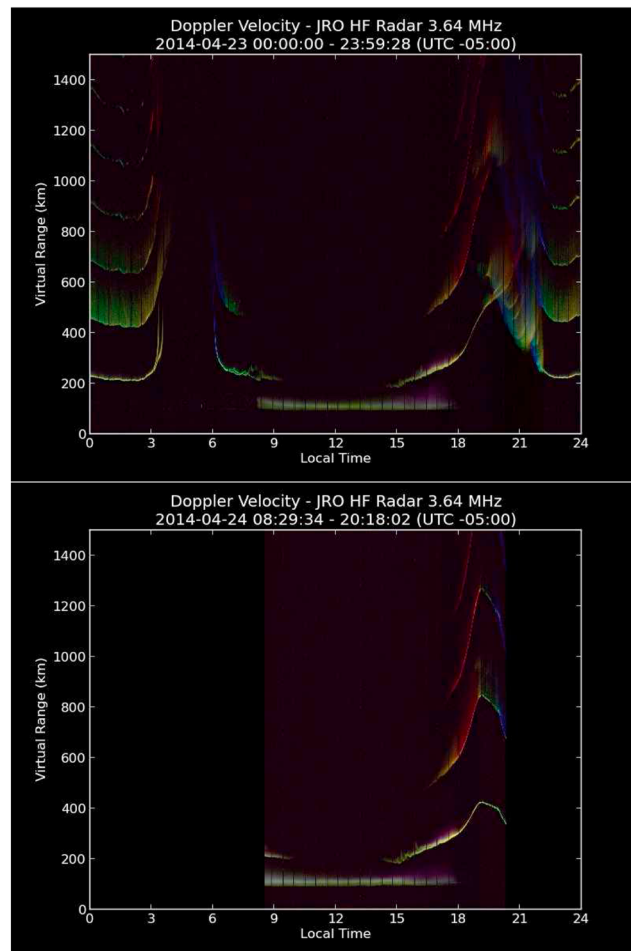


**Figure 11.** HF beacon data for the Ancon-Jicamarca link at 3.64 MHz for (top row) 23 April 2014 and (bottom row) 24 April 2014. The figures show multihop echoes versus local time and group range. The color scale indicated Doppler shifts between  $\pm 200$  m/s, with red (blue) tones indicating red (blue) shifts.

predicted by the forward model in addition to the group delay. The method can also incorporate ionospheric profile measurements from the ISR and nearby sounders. Beacon data analysis along these lines will be used in future experimental campaigns at Jicamarca and should help with the analysis of “rogue plumes” as the beacon network expands.

## 6. Analysis and Discussion

This paper reports on the third effort to anticipate the formation of ionospheric irregularities due to ESF with a numerical simulation initialized and driven by observations from Jicamarca. The irregularities are generated by what are usually called “Rayleigh Taylor” or “generalized Rayleigh Taylor” instabilities, “generalized” referring to the inclusion of currents driven by background electric fields as well as by gravity [e.g., Kelley, 1989]. This is generally a misnomer, however, since the inertial effects at the root of true Rayleigh Taylor instability play at most a small role in ESF [Zargham and Seyler, 1989]. The term “collisional interchange instability” is also sometimes applied [Zargham and Seyler, 1987], but this too is a misnomer in low-beta ionospheric plasmas where the magnetic field undergoes no significant deformation or interchange. The term “gradient drift instability” would also be misleading here since it is also commonly used to describe the instability driven by Hall currents in the electrojets [Farley, 2009].

In fact, the plasma instability mainly at work in ESF is  $E \times B$  instability or “generalized  $E \times B$ ” instability, allowing for currents driven by gravity and winds in addition to the background electric field. This is a simple instability with well-known properties. It is not thought to be turbulent in the Kolmogorov sense, the main nonlinear effect on plasma dynamics being steepening [Zargham and Seyler, 1987, 1989]. There are, however, three

subtleties which must be considered when performing analyses or simulations of ESF. First, magnetic field lines are not equipotentials in a warm plasma [Drake *et al.*, 1985], and nonequipotential field lines give rise to important dynamical behavior in the equatorial ionosphere [Aveiro and Hysell, 2012]. Specifically, they cause field-aligned tubes of plasma to rotate about magnetic field lines and contribute to shear in the bottom-side *F* region. Second, vertical currents are important in the postsunset equatorial ionosphere where the zonal plasma drifts are retrograde (opposite the direction of the winds) and may dominate zonal currents in the irregularity formation process at times [Hysell *et al.*, 2005]. Third, shear flow makes the ionospheric dynamics nonnormal, and the fastest-growing linear eigenmodes do not necessarily dominate overall irregularity growth [Flaherty *et al.*, 1999]. Capturing the contribution of transient modes on irregularity formation generally necessitates direct numerical simulation.

The simulations described in this paper incorporate empirical and physics-based models and are initialized and forced using plasma number density and drift data from Jicamarca. The simulations have been improved recently with the introduction of the new HWM-14 neutral wind model. Zonal winds from the model are tuned with a scaling factor which is set to make the observed and simulated zonal plasma drifts match at the start of the run. Meridional winds are imported from HWM-14 without scaling. Longitudinal variations in all background parameters are set to be equivalent to local-time variations. Seeding is by the inclusion of white noise at the 20% RMS level. (The noise is strong but spreads over all wave vectors. Most of the noise dissipates rapidly). The simulation code reproduces ionospheric shear flow and incorporates the effects of vertical currents and electrostatic potential variations along *B* in producing ionospheric irregularities which do exhibit transient behavior in the bottomside. The simulations are able to anticipate whether or not large plasma depletion “plumes” form and penetrate through to the topside. As the simulations have never produced “false alarms,” there appears to be no necessary condition for ESF neglected in the underlying models.

As pointed out in the earlier papers in this series, “missed detections” sometimes occur when the numerical simulations fail to predict plumes that occur under inauspicious conditions. The forecast procedure being used here so far considers only conditions proximate to the the Jicamarca radar and does not account for ESF plumes generated considerably earlier at other longitudes nor can it account for irregularities and plumes triggered by external phenomena such as pulse-like, discrete gravity waves, or MSTIDs [e.g., Krall *et al.*, 2011]. That daytime ESF exists (albeit rarely) argues strongly that depletions can be generated very far from the time and place of formation. In the future, analysis of HF beacon data should help to determine the origin(s) of the missed detections and identify processes at work regionally in addition to locally.

#### Acknowledgments

This work was supported by award FA9550-12-1-0462 from the Air Force Office of Scientific Research to Cornell University. The Jicamarca Radio Observatory is a facility of the Instituto Geofísico del Perú operated with support from NSF award AGS-1433968 through Cornell. The help of the staff is much appreciated. Data used for this publication are available through the Madrigal database.

#### References

- Aveiro, H. C., and D. L. Hysell (2010), Forecast assessment of topside spread *F* at Jicamarca, *J. Geophys. Res.*, *115*, A1233, doi:10.1029/2010JA015990.
- Aveiro, H. C., and D. L. Hysell (2012), Implications of the equipotential field line approximation for equatorial spread *F* analysis, *Geophys. Res. Lett.*, *39*, L11106, doi:10.1029/2012GL051971.
- Balan, N., K. I. Oyama, G. J. Bailey, S. Fukao, S. Watanabe, and M. A. Abdu (1997), A plasma temperature anomaly in the equatorial topside ionosphere, *J. Geophys. Res.*, *102*, 7485–7492.
- Balan, N., I. Batista, M. Abdu, J. MacDougall, and G. Bailey (1998), Physical mechanism and statistics of occurrence of an additional layer in the equatorial ionosphere, *J. Geophys. Res.*, *103*, 29,169–29,182.
- Bilitza, D., and B. W. Reinisch (2008), International reference ionosphere 2007: Improvements and new parameters, *Adv. Space Res.*, *42*, 599–609.
- Daniell, R. E., L. D. Brown, D. N. Anderson, M. W. Fox, P. H. Doherty, D. T. Decker, J. J. Sojka, and R. W. Schunk (1995), Parameterized ionospheric model: A global ionosphere parameterization based on first principles models, *Radio Sci.*, *30*, 1499–1510.
- Drake, J. F., J. D. Huba, and S. T. Zalesak (1985), Finite temperature stabilization of the gradient drift instability in barium clouds, *J. Geophys. Res.*, *90*, 5227–5234.
- Drob, D. P., et al. (2015), An update to the Horizontal Wind Model (HWM): The quiet time thermosphere, *Earth Space Sci.*, *2*, 301–319, doi:10.1002/2014EA000089.
- Farley, D. T. (2009), The equatorial E-region and its plasma instabilities: A tutorial, *Ann. Geophys.*, *27*, 1509–1520.
- Flaherty, J. P., C. E. Seyler, and L. N. Trefethen (1999), Large-amplitude transient growth in the linear evolution of equatorial spread *F* with a sheared zonal flow, *J. Geophys. Res.*, *104*, 6843–6857.
- Fu, Z. F., L. C. Lee, and J. D. Huba (1986), A quasi-local theory of the  $\mathbf{E} \times \mathbf{B}$  instability in the ionosphere, *J. Geophys. Res.*, *91*, 3263–3269.
- Guzdar, P. N., P. Satyanarayana, J. D. Huba, and S. L. Ossakow (1983), Influence of velocity shear on the Rayleigh-Taylor instability, *Geophys. Res. Lett.*, *9*, 547–550.
- Haerendel, G., J. V. Eccles, and S. Cakir (1992), Theory for modeling the equatorial evening ionosphere and the origin of the shear in the horizontal plasma flow, *J. Geophys. Res.*, *97*, 1209–1223.
- Hassam, A. B. (1992), Nonlinear stabilization of the Rayleigh-Taylor instability by external velocity shear, *Phys. Fluids*, *4*, 485.
- Hysell, D. L., and J. L. Chau (2006), Optimal aperture synthesis radar imaging, *Radio Sci.*, *41*, RS2003, doi:10.1029/2005RS003383.
- Hysell, D. L., and E. Kudeki (2004), Collisional shear instability in the equatorial *F* region ionosphere, *J. Geophys. Res.*, *109*, A11301, doi:10.1029/2004JA010636.

- Hysell, D. L., E. Kudeki, and J. L. Chau (2005), Possible ionospheric preconditioning by shear flow leading to equatorial spread F, *Ann. Geophys.*, *23*, 2647–2655.
- Hysell, D. L., R. B. Hedden, J. L. Chau, F. R. Galindo, P. A. Roddy, and R. F. Pfaff (2009), Comparing F region ionospheric irregularity observations from C/NOFS and Jicamarca, *Geophys. Res. Lett.*, *36*, L00C01, doi:10.1029/2009GL038983.
- Hysell, D. L., R. Jafari, M. A. Milla, and J. W. Meriwether (2014a), Data-driven numerical simulations of equatorial spread F in the Peruvian sector, *J. Geophys. Res. Space Physics*, *119*, 3815–3827, doi:10.1002/2014JA019889.
- Hysell, D. L., M. A. Milla, L. Condori, and J. W. Meriwether (2014b), Data-driven numerical simulations of equatorial spread F in the Peruvian sector: 2. Autumnal equinox, *J. Geophys. Res. Space Physics*, *119*, 6981–6993, doi:10.1002/2014JA020345.
- Jones, R. M., and J. J. Stephenson (1975), A versatile three-dimensional ray tracing computer program for radio waves in the ionosphere, *Tech. Rep. 75-76*, U.S. Department of Commerce, Washington, D. C.
- Kelley, M. C. (1989), *The Earth's Ionosphere*, Academic, San Diego, Calif.
- Kelley, M. C., J. J. Makela, O. de la Beaujardiere, and J. Retterer (2011), Convective ionospheric storms: A review, *Rev. Geophys.*, *49*, RG2003, doi:10.1029/2010RG000340.
- Kosarev, E. L. (1990), Shannon's superresolution limit for signal recovery, *Inverse Prob.*, *6*, 55–76.
- Krall, J., J. D. Huba, S. L. Ossakow, G. Joyce, J. J. Makela, E. S. Miller, and M. C. Kelley (2011), Modeling of equatorial plasma bubbles triggered by non equatorial traveling ionospheric disturbances, *Geophys. Res. Lett.*, *38*, L08103, doi:10.1029/2011GL046890.
- Kudeki, E., B. G. Fejer, D. T. Farley, and H. M. Ierckic (1981), Interferometer studies of equatorial F region irregularities and drifts, *Geophys. Res. Lett.*, *8*, 377–380.
- Kudeki, E., A. Akgiray, M. A. Milla, J. L. Chau, and D. L. Hysell (2007), Equatorial spread—F initiation: Post-sunset vortex, thermospheric winds, gravity waves, *J. Atmos. Sol. Terr. Phys.*, *69*(17–18), 2416–2427.
- Picone, J. M., A. E. Hedin, D. P. Drob, and A. C. Aikin (2002), NRLMSISE-00 empirical model of the atmosphere: Statistical comparisons and scientific issues, *J. Geophys. Res.*, *107*(A12), 1468, doi:10.1029/2002JA009430.
- Satyanarayana, P., P. N. Guzdar, J. D. Huba, and S. L. Ossakow (1984), Rayleigh-Taylor instability in the presence of a stratified shear layer, *J. Geophys. Res.*, *89*, 2945–2954.
- Scherliess, L., and B. G. Fejer (1999), Radar and satellite global equatorial F region vertical drift model, *J. Geophys. Res.*, *105*, 6829–6842.
- Trac, H., and U. L. Pen (2003), A primer on Eulerian computational fluid dynamics for astrophysics, *Astrophysics*, *115*, 303–321.
- Tsunoda, R. T., R. C. Livingston, and C. L. Rino (1981), Evidence of a velocity shear in bulk plasma motion associated with the post-sunset rise of the equatorial F-layer, *Geophys. Res. Lett.*, *8*, 807–810.
- Woodman, R. F. (2009), Spread F—An old equatorial aeronomy problem finally resolved?, *Ann. Geophys.*, *27*, 1915–1934.
- Woodman, R. F., and C. La Hoz (1976), Radar observations of F region equatorial irregularities, *J. Geophys. Res.*, *81*, 5447–5466.
- Zargham, S., and C. E. Seyler (1987), Collisional interchange instability: 1. Numerical simulations of intermediate-scale irregularities, *J. Geophys. Res.*, *92*, 10,073–10,088.
- Zargham, S., and C. E. Seyler (1989), Collisional and inertial dynamics of the ionospheric interchange instability, *J. Geophys. Res.*, *94*, 9009–9027.